Research
A SCIENCE PARTNER JOURNAL

RESEARCH ARTICLE

Furan Donor for NIR-II Molecular Fluorophores with Enhanced Bioimaging Performance

Chunchen Liu[1], Mengfei Li[2], Huilong Ma[1], Zhubin Hu[3], Xinyuan Wang[1], Rui Ma[1], Yingying Jiang[4], Haitao Sun[3,5*], Shoujun Zhu[2*], and Yongye Liang[1*]

[1]Department of Materials Science and Engineering, Shenzhen Key Laboratory of Printed Organic Electronics, Southern University of Science and Technology, Shenzhen 518055, China. [2]State Key Laboratory of Supramolecular Structure and Materials, College of Chemistry, Jilin University, Changchun 130012, China. [3]State Key Laboratory of Precision Spectroscopy, School of Physics and Electronic Science, East China Normal University, Shanghai 200241, China. [4]Department of Chemistry and Bio-X, Stanford University, Stanford, CA 94305, USA. [5]Collaborative Innovation Center of Extreme Optics, Shanxi University, Taiyuan, Shanxi 030006, China.

*Address correspondence to: liangyy@sustech.edu.cn (Y.L.); htsun@phy.ecnu.edu.cn (H.S.); sjzhu@jlu.edu.cn (S.Z.)

Citation: Liu C, Li M, Ma H, Hu Z, Wang X, Ma R, Jiang Y, Sun H, Zhu S, Liang Y. Furan Donor for NIR-II Molecular Fluorophores with Enhanced Bioimaging Performance. *Research* 2023;6:Article 0039. https://doi.org/10.34133/research.0039

Submitted 29 September 2022
Accepted 13 December 2022
Published 13 January 2023

Copyright © 2023 Chunchen Li et al. Exclusive Licensee Science and Technology Review Publishing House. No claim to original U.S. Government Works. Distributed under a Creative Commons Attribution License (CC BY 4.0).

The second near-infrared (NIR-II, 1,000 to 1,700 nm) molecular fluorophores containing donor–acceptor–donor conjugated backbone have attracted substantial attention due to their outstanding advantages, such as stable emission and facilely tuned photophysical properties. However, it is still challenging for them to simultaneously achieve high brightness and red-shifted absorption and emission. Herein, furan is adopted as the D unit to construct NIR-II fluorophores, demonstrating red shift of absorption, enhanced absorption coefficient, and fluorescent quantum yield when compared with the generally used thiophene counterparts. The high brightness and desirable pharmacokinetics of the optimized fluorophore, IR-FFCHP, endows improved performance for angiography and tumor-targeting imaging. Furthermore, dual-NIR-II imaging of tumor and sentinel lymph nodes (LNs) has been achieved with IR-FFCHP and PbS/CdS quantum dots, enabling the in vivo imaging navigated LN surgery in tumor-bearing mice. This work demonstrates the potential of furan for constructing bright NIR-II fluorophores for biological imaging.

Introduction

Fluorescent imaging in the second near-infrared (NIR-II, 1,000 to 1,700 nm) region processes merits of deeper penetration and higher signal-to-background ratio (SBR) than that in the visible and first near-infrared (NIR-I, 700 to 900 nm) window [1,2]. Recently, NIR-II imaging-guided liver tumor resection surgery in human has been demonstrated [3]. Fluorophores are vital for NIR-II fluorescent imaging, but their performance is generally inferior to their NIR-I counterparts [4–13]. Organic NIR-II fluorophores, including polymethine derivatives, donor–acceptor–donor (D-A-D) conjugated molecules and A-D-A conjugated molecules, have attracted tremendous attention for angiography and tumor targeting imaging due to their good biocompatibility and easily tuned photophysical properties [6,14–16]. It has been recently reported that organic fluorophores can be successfully utilized for multiplexed NIR-II imaging of sophisticated metastasis progress from tumor to sentinel lymph node (LN) [17]. To achieve improved bioimaging performance, fluorophores are expected to possess high brightness and longer absorption and emission wavelength [1–3,15,18].

Thus far, D-A-D fluorophores have been extensively studied because of their outstanding photostability and facilely tuned absorption and emission properties. Notably, a shielding unit (S, such as alkyl chain-substituted fluorene) could be introduced to weaken intermolecular interactions among conjugated backbones, resulting in improved fluorescence quantum yields (QYs) for S-D-A-D-S fluorophores [19,20]. It has also been demonstrated that rational engineering of the D unit can induce substantial tuning on the optical properties and pharmacokinetics of these fluorophores [14,21–25]. The steric size and hydrophobicity of D unit can effectively alter the backbone geometry and intermolecular interaction, which are closely correlated with the absorption or emission wavelength, QY, and absorption coefficient (ε) of fluorophores. Up to date, the D unit manipulation is generally focused on the thiophene derivatives, and considerable achievements have been realized [20,21,24]. For instance, replacing the thiophene (T) donor with 3,4-ethylenedioxy thiophene can result in conjugated backbone distortion, which can protect the A unit in the excited state and eventually afford QY enhancement. Furthermore, using alkyl thiophene as the D unit can enhance the hydrophobicity of molecules and decrease the interaction between acceptor unit and surrounding water, resulting in improved QYs in aqueous solutions [24]. However, alkyl thiophene introduction could adversely afford blue shift of absorption and

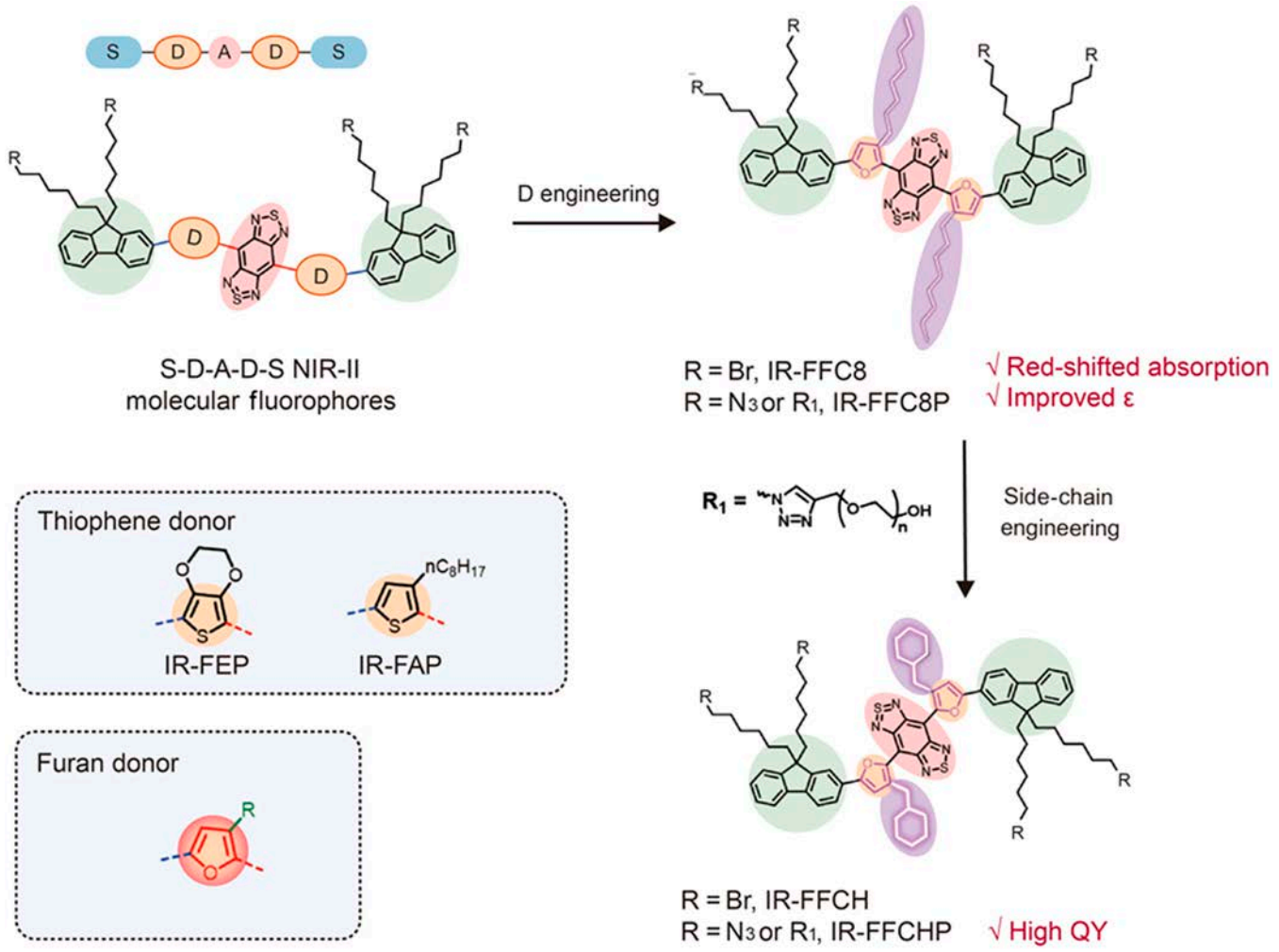
emission wavelength [26–29]. Therefore, it is urgent to find new donor units to construct highly fluorescent NIR-II fluorophores without blue-shifting the absorption wavelength.

Herein, structure optimization is adopted on the donor moiety of S-D-A-D-S fluorophores, where the furan donor is first adopted for NIR-II fluorophores because of its stronger electron donating ability than thiophene unit. The fluorophores with furan donor exhibit about 80-nm red shift of absorption and a substantial increase of ε compared to IR-FA with a thiophene donor [24]. Further, the side chains on furan donor moiety are delicately designed from *n*-octyl to 2-cyclohexylmethyl chain, forming fluorophores IR-FFC8P and IR-FFCHP, respectively. IR-FFCHP with a cyclohexyl-methyl furan donor exhibits a QY of 0.73% (QY = 0.05% of IR-26 in ethylene dichloride as the reference), which is the highest reported value for S-D-A-D-S fluorophores. Theoretical calculation results reveal that the cyclohexyl–methyl side chain can enhance protection of backbone from interaction with water without increasing molecular backbone distortion. The high brightness makes IR-FFCHP competent for in vivo whole-body angiography in mice with high resolution. Combining with PbS/CdS core/shell quantum dots (QDs) [30], dual-colored NIR-II imaging has been achieved through locating the tumor with IR-FFCHP in a NIR-IIa (1,000 to 1,300 nm) channel while mapping the sentinel LNs with QDs in a NIR-IIb (1,500 to 1,700 nm) channel, eventually enabling precise resection of sentinel LNs under high imaging contrast and depth.

Results and Discussion

Fluorophore design

As shown in Scheme 1, a strong electron-deficient unit, benzo[1,2-c:4,5-c']bis[1,2,5]thiadiazole (BBTD), is adopted as the A unit to induce a large intramolecular charger transfer effect, affording absorption and emission at a long-wavelength region [31]. Fluorene substituted with di-octyl chains is used as the shielding unit, whereas the generally used thiophene donor is replaced with the furan unit, yielding molecules IR-FFC8 and IR-FFCH. In order to enhance solubility in aqueous solutions, polyethylene glycol (PEG) chains are linked at fluorene side chain terminal through a click reaction, affording the water-soluble fluorophores IR-FFC8P and IR-FFCHP. The smaller size of oxygen atom than the sulfur atom and the stronger electron donating ability of furan are speculated to endow the fluorophores with red-shifted absorption. It is noteworthy that the 3-dimensional extending cyclohexyl-methyl chain is



Scheme. 1. Structural illustration of S-D-A-D-S fluorophores and structural regulation of molecular fluorophores in this work.

adopted to replace the *n*-octyl chain in IR-FFCH in order to substantially decrease the interaction between the conjugated backbone and the surrounding water molecules. To the best of our knowledge, it is the first attempt to adopt cyclo-alkyl side chains for NIR-II molecular fluorophores. The synthesis details of fluorophores are shown in the Supplementary Materials.

Photophysical properties

The optical properties of un-PEGylated fluorophores IR-FFC8 and IR-FFCH were first investigated via absorption and emission spectra in toluene (Fig. 1A and B and Table). Two fluorophores exhibit similar absorption peaks at about 760 nm and these are 80 nm red-shifted when compared with the thiophene counterpart IR-FA [24]. The maximum absorption coefficient (ε) of IR-FFC8 is 20.0×10^3 $M^{-1}{\cdot}cm^{-1}$, slightly higher than 17.0×10^3 $M^{-1}{\cdot}cm^{-1}$ of IR-FFCH, both of which are higher than 12.0×10^3 $M^{-1}{\cdot}cm^{-1}$ of IR-FA with the thiophene donor. Similar emission spectra with a peak at 980 to 1,010 nm and a comparable QY of ~3.0% are determined for these fluorophores in toluene.

As shown in Fig. 1C and D and Table, in the aqueous environment, 2 PEGylated fluorophores, IR-FFC8P and IR-FFCHP, show similar absorption properties with a peak at ~760 nm and ε of ~12.5×10^3 $M^{-1}{\cdot}cm^{-1}$, over 2-fold higher than that of IR-FEP (5.7×10^3 $M^{-1}{\cdot}cm^{-1}$) [24]. Impressively, IR-FFCHP (QY = 0.73%) shows much stronger fluorescent emission than IR-FEP (QY = 0.20%). It is among the highest value of the state-of-the-art QYs for S-D-A-D-S fluorophores soluble in aqueous solutions. The record high QY and ε together afford IR-FFCHP with fluorescence brightness value of 91 in water, outperforming IR-FEP [24]. Figure 1E and F illustrates the photoluminescence (PL) intensity at long-pass (LP) wavelength varying from 900 to 1,400 nm for IR-FFCHP with a low concentration in phosphate buffer saline (0.5 μM) under irradiation of an 808-nm laser. Under a high-speed exposure (5 ms), IR-FFCHP aqueous solution exhibits an outstanding PL intensity at 900-nm LP, and it decreases with increasing the LP wavelength to 1,400 nm (Fig. 1E). The fluorescence at 1,300-nm LP still could be observed presumably because of the high brightness of IR-FFCHP. With increasing the exposure time, the IR-FFCHP aqueous solution can display a comparable PL intensity at even 1,400-nm LP (Fig. 1F). Particularly, at such a low concentration (0.5 μM) and low laser power (65 mW/cm^2), comparable PL intensity at 1,300 LP can be realized with 300 ms of exposure, indicating the state-of-the-art PL performance of IR-FFCHP for water-soluble D-A-D fluorophores reported to date. The photostability of 2 fluorophores was measured under continuous laser irradiation (808 nm) for 140 min, and both fluorophores show excellent stability when compared with indocyanine green (ICG) and IR-800 CW (Fig. S1). Both fluorophores exhibit small sizes of about 10 nm from the dynamic light scattering measurement (Fig. S2).

Theoretical simulation

Firstly, the density functional theory and time-dependent density functional theory calculations were conducted to investigate molecular geometries, and optical and electronic properties of fluorophores are gained with the optimally tuned ωB97XD*/6-31G(d) method (see computational details in the Supplementary Materials) [24,32,33]. It is observed that both the 2 fluorophores possess similar electronic structures and energy levels accompanying with the whole backbones-delocalized highest occupied molecular orbitals (~ −5.80 eV) and the BBTD-localized lowest unoccupied molecular orbitals (~ −4.40 eV) (Fig. S3). The corresponding highest occupied molecular orbitals are obviously higher than that of IR-FTA (−6.20 eV), while the lowest unoccupied molecular orbitals remain almost unchanged when compared to that of IR-FTA (−4.50 eV) [21], confirming the stronger electron donating ability of furan than of thiophene unit. Additionally, these 2 fluorophores exhibit almost identical molecular backbone distortion for ground state (S_0) as well as the first singlet excited state (S_1) (Fig. S4). It is noteworthy that the dihedral angles between central BBTD and furan unit at S_o and S_1 states are calculated to be 42° and 37°, respectively, suggesting a more delocalized electronic structure of the S_1 excited state vs. the S_0 ground state. Both of them are smaller than the angles between BBTD and thiophene unit of IR-FTA (58° and 40°) [21]; the smaller distortion effect can be attributed to the smaller atom size of oxygen than sulfur, resulting in the red-shifted absorption and emission of the designed fluorophores. However, the similar electronic structures for both IR-FFC8 and IR-FFCH prompt further consideration of their states under the aqueous-solution condition.

Therefore, molecular dynamic simulations were further conducted to investigate the structural evolution of the 2 fluorophores in aqueous solutions and their interactions with surrounding water molecules [16]. Note that water has been demonstrated to reduce the fluorescence QY by more than 2 orders of magnitude and acts as an efficient fluorescence quencher for NIR-II fluorophores [21,34]. As shown in Fig. 2A, because of the alkyl chain, better molecular core protection from interaction with water molecules can be achieved for IR-FFCHP and IR-FFC8P when compared with IR-FEP. The radial distribution function (RDF) of H_2O molecules and counted H_2O number are presented in Fig. 2B and C, respectively. Both IR-FFCHP and IR-FFC8P display obviously smaller RDF values, suggesting less H_2O molecules encompassing the BBTD center than IR-FEP. It may mainly account for the higher QYs and ε of IR-FFC8P and IR-FFCHP than IR-FEP. Particularly, when compared with IR-FFC8P, benefiting from the more substantial steric hindrance of cyclohexyl group, smaller RDF and decreased water-molecule numbers can be observed for IR-FFCHP. Such a larger 3-dimensional size of cyclohexyl group can afford better protection than the *n*-octyl chain on BBTD acceptor unit as well as the whole molecular backbone from the unfavorable quenching interactions with surrounding H_2O molecules, thus endowing IR-FFCHP with a higher QY [21].

In vivo NIR-II angiography

Real-time and high-resolution angiography through a non-invasive route is helpful for studying microscopic biological processes. Current NIR angiography modality based on ICG contrast agent suffers from low imaging quality/depth and limited imaging window. The fluorophore IR-FFCHP with higher brightness was first utilized for in vivo bioimaging of vascular networks in mice. Prior to the administration of fluorophore on mice, the biocompatibility of IR-FFCHP was evaluated. The hemolysis test was conducted, and the result reveals that IR-FFCHP exhibits good blood compatibility (Fig. S5). Additionally, the cellular toxicity of IR-FFCHP was measured through standard methylthiazolyldiphenyl-tetrazolium assays, and results indicate that more than 90% of cells survived after incubation (24 h) with IR-FFCHP at a concentration up to 20 μg/ml (Fig. S6). Collectively, IR-FFCHP shows low biotoxicity.

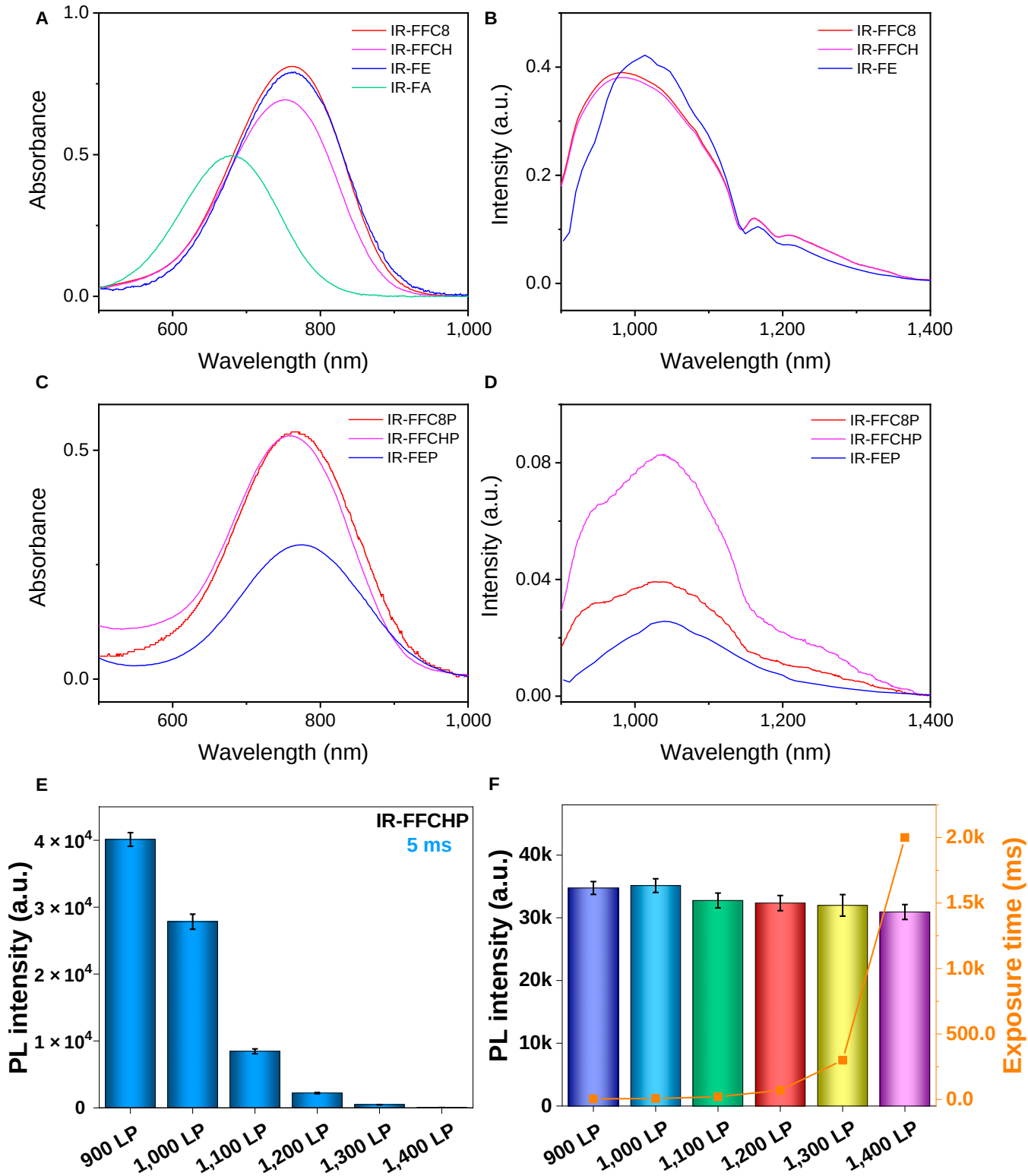


Fig. 1. Optical properties of the synthesized fluorophores. Absorption (A) and emission (B) properties of the un-PEGylated fluorophores in toluene. Absorption (C) and emission (D) properties of the PEGylated fluorophores in deionized water. Measured concentration: 4.0×10^{-5} M, excitation: 808-nm laser. Photoluminescence (PL) intensity at varied long-pass (LP) wavelength (900 to 1,400 nm) for IR-FFCHP with a low concentration in phosphate buffer saline (0.5 μM) under irradiation of a 65 mW/cm^2 laser for 5 ms (E) and increasing exposure time (F). a.u., arbitrary units.

In Fig. 3A, the whole-body vascular imaging was initially performed, and it is found that blood vessels can be clearly figured out at various positions of the mouse. After magnifying the imaging region, sophisticated vessels network in different body parts, such as back, belly, hindlimb, and foot, can be clearly discriminated (Fig. S7). The hindlimb vascular system was further scrutinized under an LP filter of 1,200 nm at different time points (Fig. 3B). High-quality imaging of hindlimb vessels

Table. Optical parameters of the fluorophores. QE (brightness value) = QY × ε. The emission of IR-FA was not measured because of its negligible absorption at 808 nm.

Fluorophore	Solvent	ε_{max} (10^3 M^{-1}·cm^{-1})	λ_{abs} (nm)	λ_{em} (nm)	Stokes shift (nm)	Φ_f (%)	QE
IR-FE[20]	Toluene	19	767	1,013	246	3.1	487
IR-FA[24]		12	680	NA	NA	N/A	NA
IR-FFC8		20.0	765	981	216	2.8	560
IR-FFCH		17.0	752	982	230	2.7	459
IR-FEP[20]	Water	5.7	780	1,047	267	0.2	11
IR-FFC8P		12.7	766	1,044	278	0.44	56
IR-FFCHP		12.5	760	1,038	278	0.73	91

N/A, not applicable

is able to be achieved at 5 min post-injection of IR-FFCHP, and considerable imaging quality can be maintained even at 6 h after injection, suggesting its long blood circulation. Figure 3C plots the SBR of the specified position of imaged hindlimb at different post-injection time points; it can be observed that highest SBR of 5.2 can be achieved at 3 h after injection. As shown in Fig. 3D, brain vessels in mice treated with ICG cannot be observed at 60 min after injection, while they can be observable for the mice treated with IR-FFCHP even at 6 h after injection, further demonstrating the long-term imaging ability of IR-FFCHP. The PL intensity and SBR changes of marked position on brain vessels for ICG and IR-FFCHP with different post-injection time points were presented in Fig. 3E and F. It can be clearly observed that the PL intensity and SBR are dramatically reduced with prolonging the post-injection time for ICG-treated mice, while SBR remains almost consistent (SBR ≈ 4) for IR-FFCHP-treated mice at even 6 h after injection. The imaging quality of cerebral and hindlimb vessels was also evaluated under different LP filters (1,000 to 1,300 nm) and exposure time (10 to 700 ms) (Figs. S8 and S9). Benefiting from the high brightness and long emission wavelength of IR-FFCHP, the tissue autofluorescence, absorption, and scattering are substantially decreased at longer wavelength region; therefore, it is found that imaging under longer LP filters can get more enhanced resolution improvement.

Pharmacokinetics and tumor-targeting imaging

After intravenous injection of IR-FFCHP into mice, the accumulation of fluorophores is mainly observed in the liver (Fig. 4A and B). Liver fluorescence signal reaches the peak at 7 d post-injection and gradually decreases to below the detectable level at 25 d post-injection (Fig. 4C), demonstrating the hepatobiliary excretion pathway of IR-FFCHP in mice. After injecting IR-FFCHP in 4T1 tumor-bearing mice, the long blood circulation of IR-FFCHP enables effective passive tumor targeting ability (Fig. 4B). The tumor signal gradually increases from 5 min post-injection of IR-FFCHP and reaches the peak at 48 h, which subsequently decreases until 7 d post-injection (Fig. 4D). It is plausible that the long circulation of IR-FFCHP in mice can improve the enhanced permeability and retention (EPR) effect and lead to high-quality tumor-targeting imaging [35]. The biodistribution of IR-FFCHP in different organs was further investigated through the imaging of surgically separated organs, and the result reveals that the fluorophore is mainly accumulated in liver and tumor (Fig. 4E and F), once again demonstrating the hepatobiliary metabolization pathway and EPR-assisted tumor accumulation of IR-FFCHP.

Dual-colored NIR-II imaging-guided surgery

Resection of tumor tissues is the main strategy for cancer treatment. Considering that the sentinel LNs are the principal pathway in tumor metastasis, which is closely related with tumor prognosis, tumor staging identification, and treatment decision [35], it is of vital importance to concurrently visualize the metastasis of tumor in sentinel LNs during the imaging navigated tumor excision in clinical applications [35]. Here, we used the IR-FFCHP for tumor NIR-IIa (1,000 to 1,500 nm) imaging because of its high fluorescence brightness and intense retention in tumor. In order to achieve dual-colored imaging, PbS/CdS QDs were utilized for NIR-IIb (1,500 to 1,700 nm) imaging of tumor-associated sentinel LNs [30]. We initially attempted to investigate the NIR-IIb imaging of the QDs for mouse hindlimb LNs (Fig. S10). Two mice footpads were intradermally injected with IR-FFCHP and QDs, respectively. It can be observed that the signal of IR-FFCHP cannot be detected with an LP filter of 1,500 nm, indicating the nonoverlapping dual-colored imaging between sentinel LNs using QDs and tumor with IR-FFCHP. Therefore, dual-colored bioimaging can be successfully conducted. At 24 h post-administration of IR-FFCHP, the QDs were intratumorally injected, and the tumor and LN signals can both reach the optimal intensity at 26 h post-injection (Fig. 5A and C and Fig. S11). The tumor can be figured out within an NIR-IIa window, while the cancer-associated LNs can be discriminated in an NIR-IIb window, respectively. With the help of dual-colored imaging, the resection surgery of tumor and sentinel LNs was successfully accomplished (Fig. 5B). The hematoxylin and eosin (H&E) stain of the resected tumor and LNs with/without tumor metastasis is illustrated in Fig. 5D, and the result further demonstrates the accomplishment of precise resection surgery under dual-colored NIR-II imaging. Additionally, organs in normal and 4T1 tumor-bearing mice were also treated with the H&E stain method, and the results verify the in vivo biocompatibility of IR-FFCHP (Fig. S12).

Conclusion

In summary, furan is adopted for the first time as the D unit to construct 2 S-D-A-D-S fluorophores, IR-FFC8P and IR-FFCHP. Compared to thiophene counterparts, stronger electron donating

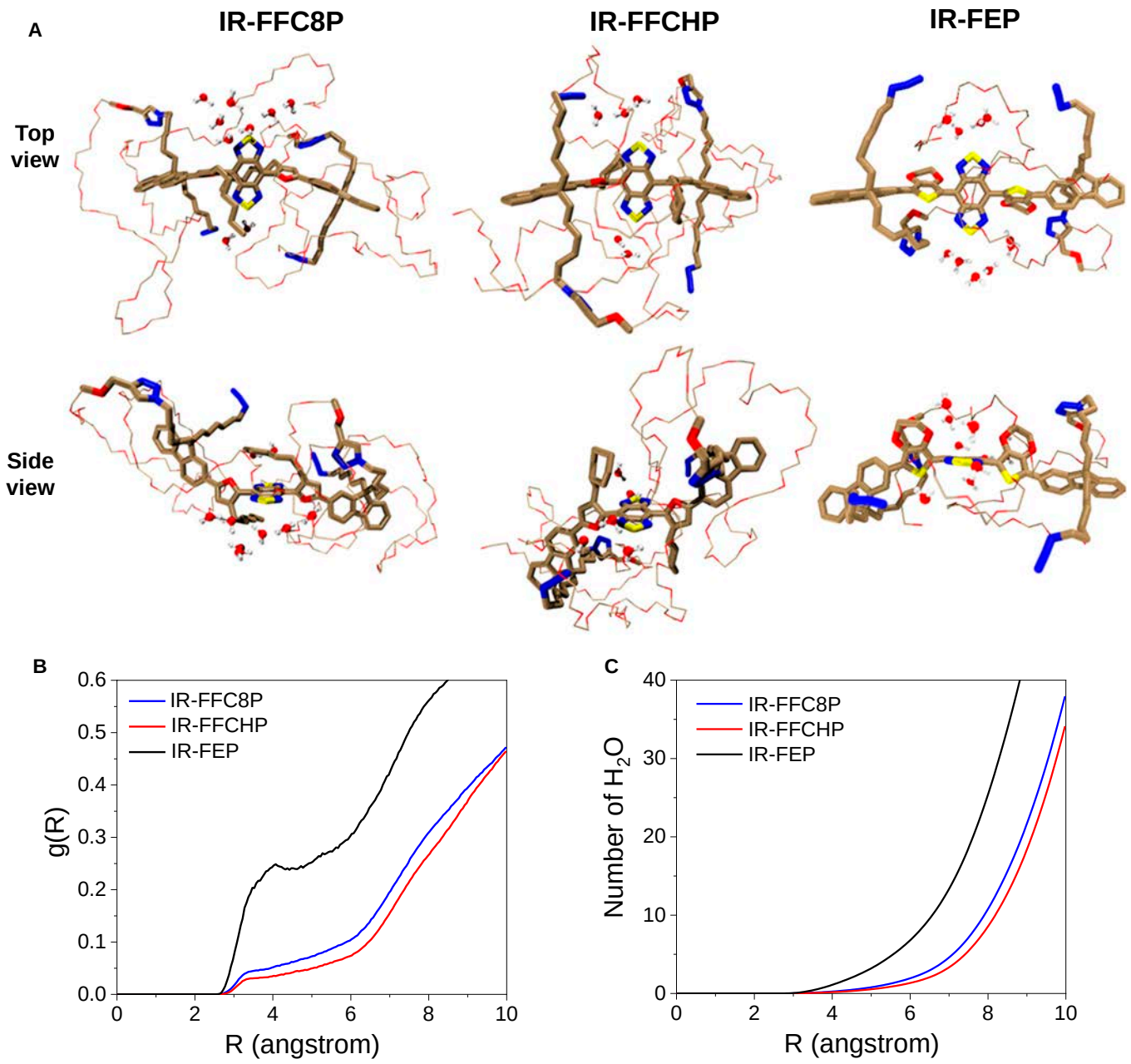


Fig. 2. Molecular dynamic simulations of the fluorophores. (A) Schematic diagram of interaction between H_2O and fluorophores in aqueous circumstances through molecular dynamic simulations. Brown, red, yellow, blue, and thin line parts with gray and red represent the C, O, S, N, and PEG chain, respectively. (B) RDF of O atoms from water around the BBTD of fluorophores with the radius (angstrom) around BBTD core. (C) Counted H_2O number surrounding BBTD.

ability and smaller size of oxygen atom together endow the furan fluorophores with a stronger intramolecular charger transfer effect and less molecular backbone distortion, resulting in red-shifted absorption and enhanced absorption coefficient. The Cyclohexyl–methyl side chain on a furan donor can afford better protection on a BBTD unit from unfavorable quenching interaction with surrounding water molecules without increasing conjugated backbone distortion, affording IR-FFCHP with the record-high QY of 0.73% for reported S-D-A-D-S structural fluorophores. In addition to high brightness, IR-FFCHP also exhibits long blood circulation in mice, enabling better brain vascular imaging than clinical ICG and intense tumor retention. Combined with NIR-IIb QDs, dual-colored NIR-II imaging using IR-FFCHP to mark tumors and QDs to distinguish sentinel LNs is demonstrated, which enables the in vivo imaging-navigated surgery of LNs in 4T1 tumor-bearing mice. This work provides new insights for developing high-performance NIR-II molecular fluorophores through delicate molecular engineering strategies, which is expected to accelerate the application of NIR-II fluorophores in sophisticated in vivo imaging. This furan donor modification strategy can also be utilized for constructing donor–acceptor conjugated polymers with strong absorption in NIR-II windows and high photothermal conversion efficiency for deep-brain neuromodulation and other related applications [36].

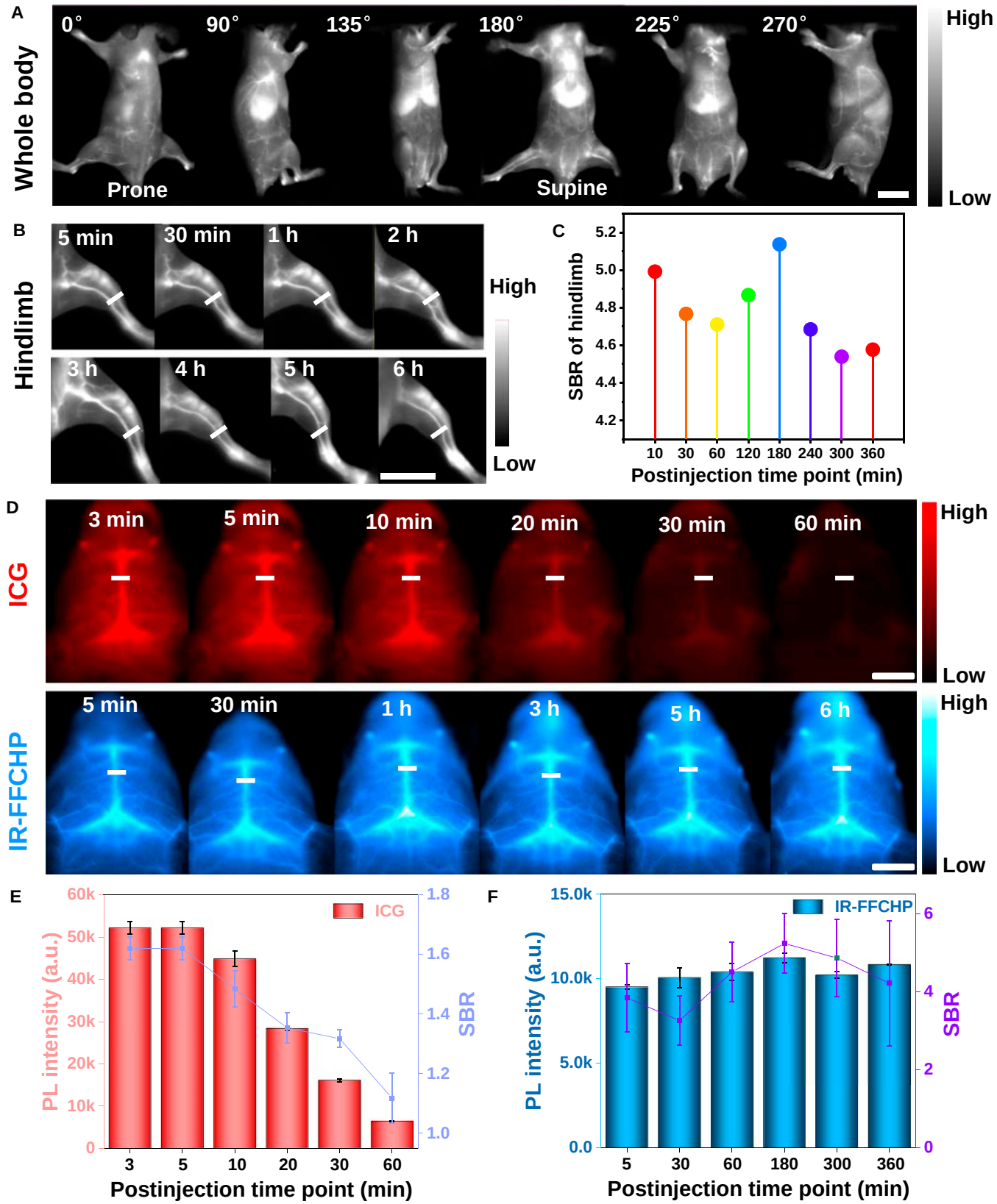


Fig. 3. Imaging performance of the fluorophores. Vessels imaging for the whole-body (A) and magnified hindlimb (B). (C) The signal-to-background ratio (SBR) of the specified position of imaged hindlimb at different post-injection time points. (D) Brain vessel imaging in mice treated with indocyanine green (ICG) and IR-FFCHP. The PL intensity and SBR changes of marked position on brain vascular for ICG (E) and IR-FFCHP (F) with different post-injection time points. Intravenous injection dose: 100 μl, 1 mg/ml; LP filter: 1,200 nm; exposure time: 200 ms; excitation: 808-nm laser (80 mW/cm^2). The scale bars represent 1 cm.

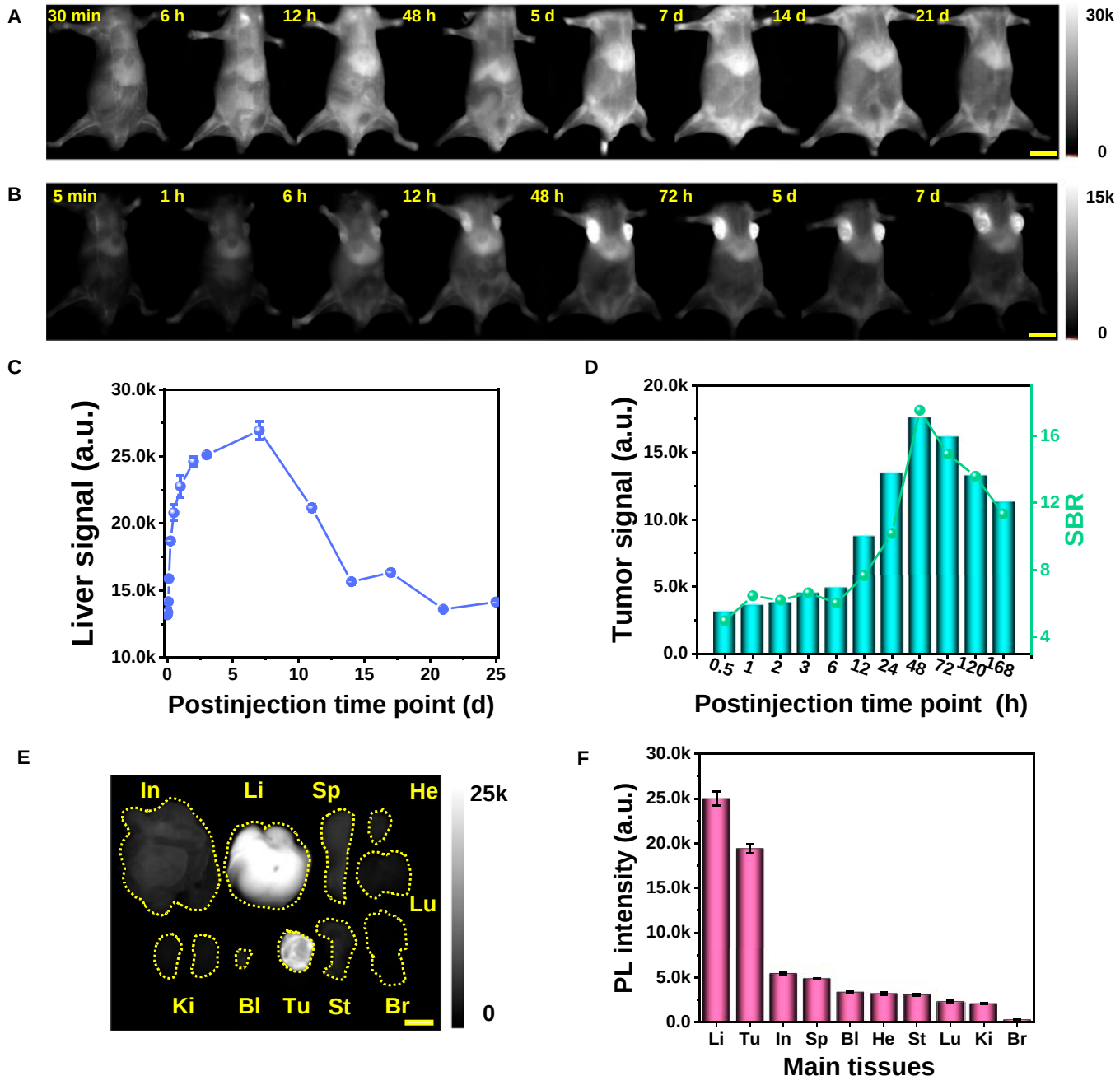


Fig. 4. Pharmacokinetics and targeted imaging of 4T1 tumor model with IR-FFCHP. (A) In vivo circulation of IR-FFCHP. (B) Imaging of a mouse with 4T1 tumor after intravenous injection of IR-FFCHP; the high EPR effect on 4T1 tumor is observed because of the long circulation of fluorophores. The corresponding fluorescence signal intensity of liver (C) and tumor (D) as a function of time. (E) Ex vivo imaging of main organs of IR-FFCHP-treated mice after 7 d post-injection. (F) The fluorescence intensity values of main organs of IR-FFCHP treated mice. Imaging condition: 1,200-nm LP, 100-ms exposure time, 80 mW/cm^2 laser power. The scale bars represent 1 cm. In, intestine; Li, liver; Sp, spleen; He, heart; Lu, lung; Ki, kidney; Bl, bladder; Tu, tumor; St, stomach; Br, brain.

Acknowledgments

Funding: The authors acknowledge the support from the National Natural Science Foundation of China (Nos. 21772084 and 12034008), Fundamental Research Layout of Shenzhen (No. JCY20180504165657443), Guangdong Provincial Natural Science Foundation-Yueshen Joint Funding (Youth Project) (No. 2019A1515110464), and the Shenzhen Science and Technology Commission-free exploration/general project (No. JCYJ20190812151209348). Special fund for local science and technology development guided by central government is acknowledged. The support from Shanghai Rising Star Program (No. 21QA1402600) and the graduate fellowship (201808440345) from Chinese Scholarship Council are also acknowledged. The NIR-II small animal fluorescence imaging system (DeepVision, Nirmidas Biotech) is acknowledged. **Author contributions**: C.L. contributed in data analysis, preparation, and manuscript writing. M.L. contributed to bioimaging works. H.M. contributed to compound synthesis. Y.J. helped in the bioimaging works. Z.H. and H.S. conducted the theoretical calculations. S.Z. supervised the in vivo NIR-II imaging. X.W. and R.M. helped with the data analysis. All works were under the supervision

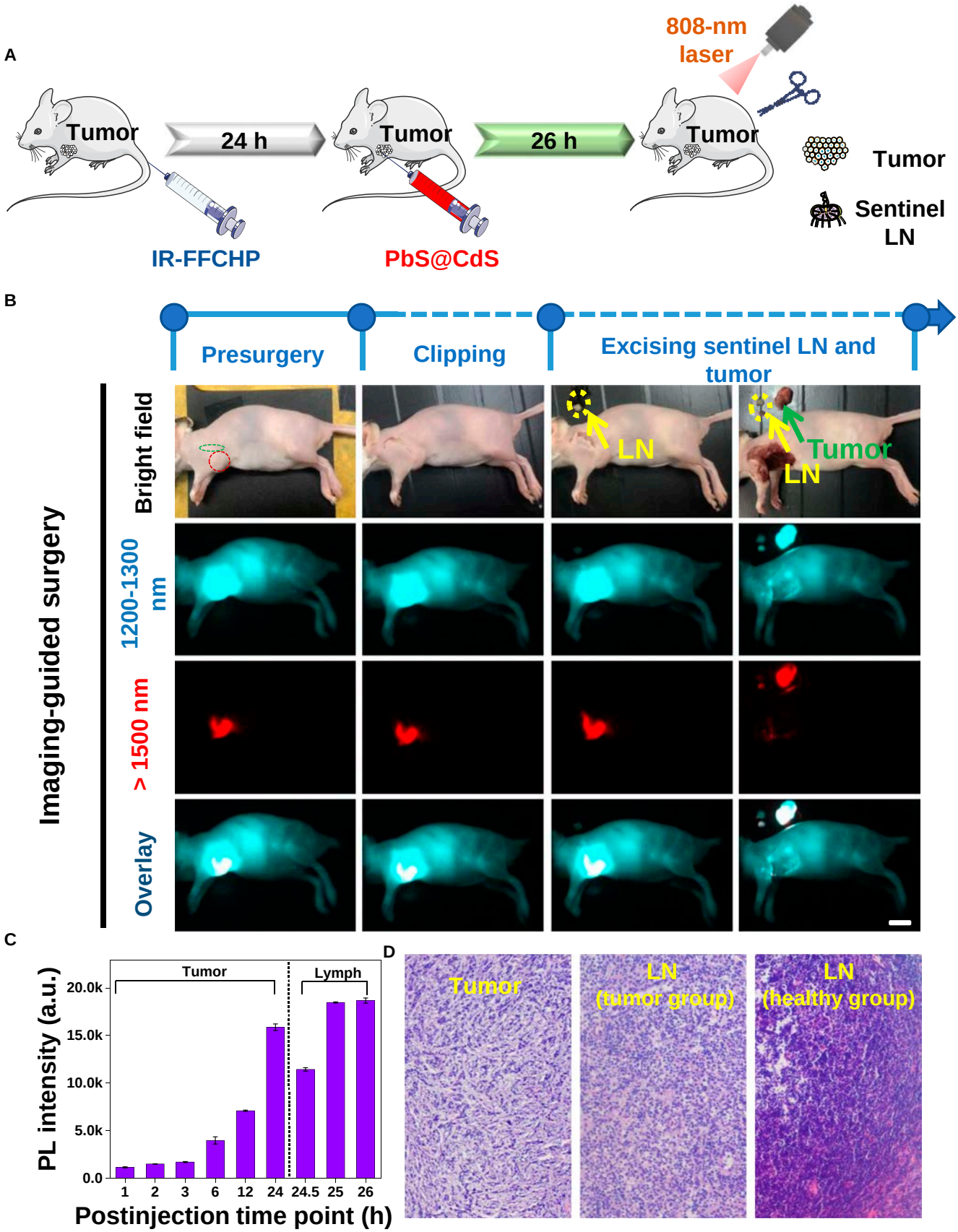


Fig. 5. NIR-II imaging guided surgery with IR-FFCHP. (A) The schematic illustration of dual-colored in vivo NIR-II imaging guided 4T1 tumor-sentinel LN surgery. (B) Tumor imaging with IR-FFCHP in 1,200- to 1,300-nm window and sentinel LN imaging with QDs in >1,500-nm window. (C) PL intensity of tumor and LN at different time points after sequential injection of IR-FFCHP and QDs. (D) H&E stain of the resected tumor and LNs with/without tumor metastasis. The scale bar represents 1 cm.

of Y.L. All authors contributed to the article and approved the submission. C.L., M.L., and H.M. contributed equally to this work. **Competing interests**: The authors declare that they have no competing interests.

Data Availability

The data used to support the findings of this study are available from the corresponding authors upon request.

Supplementary Materials

Methods.
Figs. S1 to S12.
Tables S1 and S2.

References

1. Hong G, Antaris AL, Dai H. Near-infrared fluorophores for biomedical imaging. *Nature Biomedical Engineering*. 2017;1(1):0010.
2. Zhu S, Tian R, Antaris AL, Chen X, Dai H. Near-infrared-II molecular dyes for cancer imaging and surgery. *Adv Mater*. 2019;31(24):1900321.
3. Hu Z, Fang C, Li B, Zhang Z, Cao C, Cai M, Su S, Sun X, Shi X, Li C, et al. First-in-human liver-tumour surgery guided by multispectral fluorescence imaging in the visible and near-infrared-I/II windows. *Nat Biomed Eng*. 2020;4(3):259–271.
4. Feng Y, Zhu S, Antaris AL, Chen H, Xiao Y, Lu X, Jiang L, Diao S, Yu K, Wang Y, et al. Live imaging of follicle stimulating hormone receptors in gonads and bones using near infrared II fluorophore. *Chem Sci*. 2017;8(5):3703–3711.
5. Antaris AL, Chen H, Diao S, Ma Z, Zhang Z, Zhu S, Wang J, Lozano AX, Fan Q, Chew L, et al. A high quantum yield molecule-protein complex fluorophore for near-infrared II imaging. *Nat Commun*. 2017;8(1):15269.
6. Antaris AL, Chen H, Cheng K, Sun Y, Hong G, Qu C, Diao S, Deng Z, Hu X, Zhang B, et al. A small-molecule dye for NIR-II imaging. *Nat Mater*. 2016;15(2):235–242.
7. Wang R, Li X, Zhou L, Zhang F. Epitaxial seeded growth of rare-earth nanocrystals with efficient 800 nm near-infrared to 1525 nm short-wavelength infrared downconversion photoluminescence for in vivo bioimaging. *Angew Chem Int Ed*. 2014;53(45):12086–12090.
8. Welsher K, Liu Z, Sherlock SP, Robinson JT, Chen Z, Daranciang D, Dai H. A route to brightly fluorescent carbon nanotubes for near-infrared imaging in mice. *Nat Nanotechnol*. 2009;4(11):773–780.
9. Sun Y, Ding M, Zeng X, Xiao Y, Wu H, Zhou H, Ding B, Qu C, Hou W, Er-bu AGA, et al. Novel bright-emission small-molecule NIR-II fluorophores for in vivo tumor imaging and image-guided surgery. *Chem Sci*. 2017;8(5):3489–3493.
10. Du Y, Xu B, Fu T, Cai M, Li F, Zhang Y, Wang Q. Near-infrared photoluminescent Ag_2S quantum dots from a single source precursor. *J Am Chem Soc*. 2010;132(5):1470–1471.
11. Hong G, Zou Y, Antaris AL, Diao S, Wu D, Cheng K, Zhang X, Chen C, Liu B, He Y, et al. Ultrafast fluorescence imaging in vivo with conjugated polymer fluorophores in the second near-infrared window. *Nat Commun*. 2014;5:4206.
12. Li D, Qu C, Liu Q, Wu Y, Hu X, Qian K, Chang B, He S, Yuan Y, Li Y, et al. Monitoring the real-time circulatory system-related physiological and pathological processes in vivo using a multifunctional NIR-II probe. *Adv Funct Mater*. 2020;30(6):1906343.
13. Franke D, Harris DK, Chen O, Bruns OT, Carr JA, MWB W, Bawendi MG. Continuous injection synthesis of indium arsenide quantum dots emissive in the short-wavelength infrared. *Nat Commun*. 2016;7:12749.
14. Wan H, Ma H, Zhu S, Wang FF, Tian Y, Ma R, Yang Q, Hu Z, Zhu T, Wang W, et al. Developing a bright NIR-II fluorophore with fast renal excretion and its application in molecular imaging of immune checkpoint PD-L1. *Adv Funct Mater*. 2018;28(50):1804956.
15. Wan H, Yue J, Zhu S, Uno T, Zhang X, Yang Q, Yu K, Hong G, Wang J, Li L, et al. A bright organic NIR-II nanofluorophore for three-dimensional imaging into biological tissues. *Nat Commun*. 2018;9(1):1171.
16. Zhu X, Liu C, Hu Z, Liu H, Wang J, Wang Y, Wang X, Ma R, Zhang X, Sun H, et al. High brightness NIR-II nanofluorophores based on fused-ring acceptor molecules. *Nano Res*. 2020;13(9):2570–2575.
17. Tian R, Ma H, Zhu S, Lau J, Ma R, Liu Y, Lin L, Chandra S, Wang S, Zhu X, et al. In vivo imaging: Multiplexed NIR-II probes for lymph node-invaded cancer detection and imaging-guided surgery. *Adv Mater*. 2020;32(11):2070086.
18. Li C, Chen G, Zhang Y, Wu F, Wang Q. Advanced fluorescence imaging technology in the near-infrared-II window for biomedical applications. *J Am Chem Soc*. 2020;142(35):14789–14804.
19. Zhu S, Yang Q, Antaris AL, Yue J, Ma Z, Wang H, Huang W, Wan H, Wang J, Diao S, et al. Molecular imaging of biological systems with a clickable dye in the broad 800- to 1,700-nm near-infrared window. *Proc Natl Acad Sci USA*. 2017;114(5):962–967.
20. Yang Q, Ma Z, Wang H, Zhou B, Zhu S, Zhong Y, Wang J, Wan H, Antaris A, Ma R, et al. Rational design of molecular fluorophores for biological imaging in the NIR-II Window. *Adv Mater*. 2017;29(12):1605497.
21. Yang Q, Hu Z, Zhu S, Ma R, Ma H, Ma Z, Wan H, Zhu T, Jiang Z, Liu W, et al. Donor engineering for NIR-II molecular fluorophores with enhanced fluorescent performance. *J Am Chem Soc*. 2018;140(5):1715–1724.
22. Tian R, Ma H, Yang Q, Wan H, Zhu S, Chandra S, Sun H, Kiesewetter DO, Niu G, Liang Y, et al. Rational design of a super-contrast NIR-II fluorophore affords high-performance NIR-II molecular imaging guided microsurgery. *Chem Sci*. 2019;10(1):326–332.
23. Zhang X-D, Wang H, Antaris AL, Li L, Diao S, Ma R, Nguyen A, Hong G, Ma Z, Wang J, et al. Traumatic brain injury imaging in the second near-infrared window with a molecular fluorophore. *Adv Mater*. 2016;28(32):6872–6879.
24. Ma H, Liu C, Hu Z, Yu P, Zhu X, Ma R, Sun Z, Zhang CH, Sun H, Zhu S, et al. Propylenedioxy thiophene donor to achieve NIR-II molecular fluorophores with enhanced brightness. *Chem Mater*. 2020;32(5):2061–2069.
25. Liu C, Ma H, Hu Z, Tian R, Ma R, Xu Y, Wang X, Zhu X, Yu P, Zhu S, et al. Shielding unit engineering of NIR-II molecular fluorophores for improved fluorescence performance and renal excretion ability. *Front Chem*. 2021;9:715.

26. Li B, Lu L, Zhao M, Lei Z, Zhang F. An efficient 1064 nm NIR-II excitation fluorescent molecular dye for deep-tissue high-resolution dynamic bioimaging. *Angew Chem Int Ed*. 2018;57(25):7483–7487.
27. Sun C, Li B, Zhao M, Wang S, Lei Z, Lu L, Zhang H, Feng L, Dou C, Yin D, et al. J-aggregates of cyanine dye for NIR-II in vivo dynamic vascular imaging beyond 1500 nm. *J Am Chem Soc*. 2019;141(49):19221–19225.
28. Li B, Zhao M, Feng L, Dou C, Ding S, Zhou G, Lu L, Zhang H, Chen F, Li X, et al. Organic NIR-II molecule with long blood half-life for in vivo dynamic vascular imaging. *Nat Commun*. 2020;11(1):3102.
29. Lu L, Li B, Ding S, Fan Y, Wang S, Sun C, Zhao M, Zhao C-X, Zhang F. NIR-II bioluminescence for in vivo high contrast imaging and in situ ATP-mediated metastases tracing. *Nat Commun*. 2020;11(1):4192.
30. Zhang M, Yue J, Cui R, Ma Z, Wan H, Wang F, Zhu S, Zhou Y, Kuang Y, Zhong Y, et al. Bright quantum dots emitting at ∼1,600 nm in the NIR-IIb window for deep tissue fluorescence imaging. *Proc Natl Acad Sci USA*. 2018;115(26):6590–6595.
31. Qian G, Dai B, Luo M, Yu D, Zhan J, Zhang Z, Ma D, Wang ZY. Band gap tunable, donor−acceptor−donor charge-transfer heteroquinoid-based chromophores: Near infrared photoluminescence and electroluminescence. *Chem Mater*. 2008;20(19):6208–6216.
32. Chai J-D, Head-Gordon M. Long-range corrected hybrid density functionals with damped atom–atom dispersion corrections. *Phys Chem Chem Phys*. 2008;10(44):6615–6620.
33. Sun H, Zhong C, Brédas J-L. Reliable prediction with tuned range-separated functionals of the singlet–triplet gap in organic rmitters for thermally sctivated delayed fluorescence. *J Chem Theory Comput*. 2015;11(8):3851–3858.
34. Maillard J, Klehs K, Rumble C, Vauthey E, Heilemann M, Fürstenberg A. Universal quenching of common fluorescent probes by water and alcohols. *Chem Sci*. 2021;12(4):1352–1362.
35. Tian R, Ma H, Zhu S, Fan Y, Wang S, Sun C, Zhao M, Zhao C-X, Zhang F, et al. Multiplexed NIR-II probes for lymph node-invaded cancer detection and imaging-guided surgery. *Adv Mater*. 2020;32(11):1907365.
36. Wu X, Jiang Y, Rommelfanger NJ, Yang F, Zhou Q, Yin R, Liu J, Cai S, Ren W, Shin A, et al. Tether-free photothermal deep-brain stimulation in freely behaving mice via wide-field illumination in the near-infrared-II window. *Nat Biomed Eng*. 2022;6(6):754–770.